Eur. Phys. J. E (2015) **38**: 17
DOI 10.1140/epje/i2015-15017-4

THE EUROPEAN PHYSICAL JOURNAL E

Regular Article

Direct imaging of long-range concentration fluctuations in a ternary mixture*

Direct imaging of ternary mixtures

Ana Oprisan[1,a], Sorinel A. Oprisan[1], John J. Hegseth[2], Yves Garrabos[3], Carole Lecoutre[3], and Daniel Beysens[4,5]

[1] Department of Physics and Astronomy, College of Charleston, Charleston, SC 29424, USA
[2] Department of Physics, University of New Orleans, New Orleans, LA 70148, USA
[3] CNRS, ICMCB, ESEME, UPR 9048, F-33600 Pessac, France and Univ. Bordeaux, ICMCB, UPR 9048, F-33600 Pessac, France
[4] Service des Basses Températures, UMR-E CEA/UJF-Grenoble 1, INAC, Grenoble, France
[5] Physique et Mécanique des Milieux Hétérogènes, UMR 7636 CNRS - ESPCI - Université Pierre et Marie Curie - Université Paris Diderot, 10 rue Vauquelin, 75005 Paris, France

Received 3 July 2014 and Received in final form 10 November 2014
Published online: 20 March 2015 –

Abstract. We used a direct imaging technique to investigate concentration fluctuations enhanced by thermal fluctuations in a ternary mixture of methanol (Me), cyclohexane (C), and partially deuterated cyclohexane (C*) within 1 mK above its consolute critical point. The experimental setup used a low-coherence white-light source and a red filter to visualize fluctuation images. The red-filtered images were analyzed off-line using a differential dynamic microscopy algorithm that allowed us to determine the correlation time, τ, of concentration fluctuations. From τ, we determined the mutual mass diffusion coefficient, D, very near and above the critical point of Me-CC* mixtures. We also numerically estimated both the background and critical contributions to D and compared the results against our experimental values determined from τ. We found that the experimental value of D is close to the prediction based on Stokes-Einstein diffusion law with Kawasaki's correction.

1 Introduction

In this work, we determined the mutual mass diffusion coefficient, D, for a density-matched ternary mixture of methanol (Me), cyclohexane (C), and partially deuterated cyclohexane (C*) within 1 mK above its consolute critical point using a microscopy direct imaging setup.

Critical fluctuations in density-matched systems

A strong limiting factor in fluctuation visualization near critical point is the gravitational field that leads to sedimentation and convection, which reduce both the duration and the spatial extent of critical fluctuations. One possible solution is to use a density-matched mixture such that the density of one phase is as close as possible to the density of the other phase. In this work, we used a density-matched ternary mixture of methanol (Me), cyclohexane (C) and deuterated cyclohehane (C*). Since the density of methanol ($\rho_{\mathrm{Me}} = 0.78647\,\mathrm{g/cm^3}$) is slightly larger than that of cyclohexane ($\rho_C = 0.77354\,\mathrm{g/cm^3}$), methanol and cyclohexane (Me-C) system can be initially prepared with nearly matched densities. By adding a small amount of deuterated cyclohexane (C*), which has a density larger than that of methanol ($\rho_{\mathrm{C}^*} = 0.88717\,\mathrm{g/cm^3}$), it is possible to create a density-matched system of Me-CC* [1] such that the density of C+C* phase matches the density of methanol by tuning the density difference between methanol and cyclohexane. In Me-CC* mixtures, the density difference between methanol and cyclohexane is tunable via the deuteration ratio C*/(C*+C). Furthermore, the value of thermal expansion coefficient of methanol ($\alpha_{\mathrm{Me}} = -1.20 \cdot 10^{-3}\,\mathrm{K^{-1}}$) is close to that of cyclohexane ($\alpha_{\mathrm{C}} = -1.27 \cdot 10^{-3}\,\mathrm{K^{-1}}$), which would allow maintaining the density match over a relatively wide range of temperatures. To our knowledge, the only Earth-based experiment that investigated Me-CC* mixtures near the consolute critical point was performed by Houessou *et al.* [1].

Using a microscopy imaging method, we carried out experiments with such a Me-CC* mixture to investigate concentration fluctuations within 1 mK above its consolute critical point and to estimate the mutual mass diffusion coefficient D of this ternary mixture (see sect. 2).

* Contribution to the Topical Issue "Thermal non-equilibrium phenomena in multi-component fluids" edited by Fabrizio Croccolo and Henri Bataller.

[a] e-mail: oprisana@cofc.edu

Universality classes

Houessou *et al.* [1] showed that the ternary mixture of methanol (Me), cyclohexane (C), and deuterated cyclohexane (C*) has the same critical behavior as the binary mixture Me-C. For example, the critical exponent $\beta_{\text{Me-CC}^*} = 0.322 \pm 0.002$ in Me-CC* critical mixtures, although slightly smaller than in critical Me-C binary mixture ($\beta_{\text{Me-C}} = 0.334 \pm 0.004$), it is close to the theoretically predicted value $\beta = 0.325$. Beysens *et al.* [2] carried out a similar experiment using the ternary mixture Me-CC* under microgravity conditions and also found that it behaves as the binary mixture Me-C with respect to the phase transition phenomena. For example, based on measurements of both the osmotic susceptibility, χ, and the correlation length, ξ, at criticality, they established that the ternary mixtures Me-CC* belongs to the same universality class as the binary mixture Me-C. Furthermore, they found that their microgravity experiments with density-matched Me-CC* mixtures gave the same results as the Earth-based experiments carried out by Houessou *et al.* [1]. Critical behavior and scaling exponents obtained with density-matched Me-CC* mixtures [1,2] also match the results obtained by Knobler and Wong [3] with density-matched binary mixtures of isobutyric acid and water near their consolute critical point. These findings support the conclusion that the ternary mixture of Me-CC* and binary mixtures belong to the same universality class of the so-called 3D-uniaxial Ising-like systems [4].

Order parameter

Second-order phase transitions are characterized by a continuous first derivative of Gibbs free energy and an order parameter, M, that describes the degree of order of the thermodynamic system that undergoes such a transition [4,5]. As shown by Griffiths and Wheeler [6], an appropriate choice of the order parameter in binary mixtures near a liquid-liquid consolute critical point is the distance to critical concentration c_c, *i.e.* $M = \Delta c = c - c_c$ (at constant pressure). A fluid mixture consists of partially miscible (soluble) components below a certain (critical) temperature, T_c, and completely miscible above it. Above T_c, thermal motion prevents phase separation to occur and the system is homogeneous. When the temperature, T, approaches its critical value, T_c, it is convenient to use the reduced temperature, $\epsilon = |T - T_c|/T_c$, to express the temperature dependence of thermophysical properties as well-known power laws. For example, near T_c, the fluctuation correlation length, ξ, scales as $\xi_0 \epsilon^{-\nu}$, with $\nu = 0.63$ [7–9]. Critical exponents, such as the correlation length critical index, ν; and the system-dependent amplitudes, such as the correlation length constant, ξ_0, have been determined in various ways, especially for the Me-CC* case [1]. We used such power laws for mutual mass diffusion coefficient D within 1 mK above its consolute critical point to compare our experimentally determined D_{exp} against theoretical predictions (see sect. 4).

Direct imaging

Large and correlated fluctuations of the order parameter take place at critical point. Such fluctuations cover length scales from atomic level to microns and are determined by the distance to the critical point according to the scaling law $\xi = \xi_0 \epsilon^{-\nu}$. At the same time, the spectrum of relaxation times of critical fluctuations range from microscopic times (10^{-12} s) up to a 10^3 s. Fluctuations can be probed experimentally using direct imaging or light scattering techniques [10,11]. Direct imaging techniques deliver detailed information on the local structure and dynamics of the sample by providing access to real space images. Scattering techniques provide a statistical characterization of the sample as a whole in the reciprocal (Fourier) space through the angular and time dependence of the scattered light intensity. Usually, direct imaging methods use non-coherent white-light sources, while scattering experiments use lasers since a certain degree of coherence of the light source is required. Some experimental setups combined direct imaging with dynamic light scattering (DLS) and took advantage of the complementary information provided by the two techniques [12,13]. Visualization of microscopic fluctuation through direct imaging can be achieved by using a standard white-light microscope and a digital video camera [10–13]. Fourier analysis of recorded images allows access to statistical information regarding sample dynamics [10,11]. The microscopy method that combined direct imaging with light scattering was called differential dynamic microscopy (DDM) [10,11]. The DDM technique has been extensively used, for example, to improve the conventional video tracking method for bacteria [14,15], was combined with confocal microscopy for fluorescent samples to access statistical information regarding the dynamics of samples [16], and was applied to anisotropic colloidal suspensions to extract orientational order parameter and diffusion coefficients [17].

In this work, we used a microscopy direct imaging method with a low-coherence white-light source and a CCD camera to record concentration fluctuations near the consolute critical point of Me-CC* (see sect. 3). The experimental setup of the direct imaging technique used here is similar with the standard DMM [10,11]. We performed off-line analysis of time sequences of fluctuating images using Fourier transforms to extract quantitative information on the dynamics of the system, such as the mutual mass diffusion coefficient.

2 Experimental setup

Sample cell unit and mixing

Me-CC* mixture was placed between two 8.5 mm thick and 10 mm diameter sapphire windows separated by a gold-coated 3 mm thick brass spacer [18,19]. The sample was placed in a larger copper housing of diameter 6 cm and length 6 cm. The copper housing of the cell contains

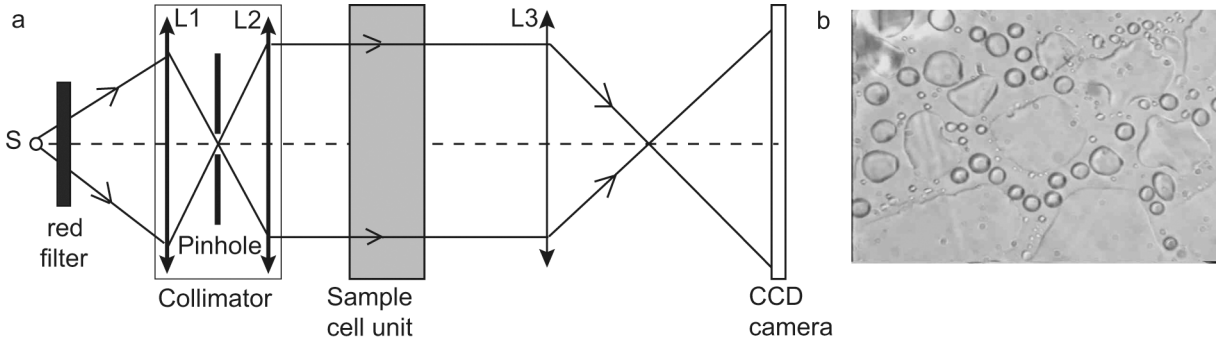

Fig. 1. (a) The optical microscopy setup used for direct imaging of Me-CC* ternary mixture (not to scale). A halogen white-light source and a collimator (lenses L_1 and L_2) produced a beam of light that was focused by an achromatic high-quality Olympus Zuiko 50 mm f/1.8 compound lens (L_3) on a Sony XC-75CE CCD camera. Concentration fluctuations in the sample scattered the beam of light producing fluctuation in the recorded light intensity. (b) Direct imaging of phase-separated Me-CC* using bright field technique without the red filter.

two thermistors for temperature measurement and control. To avoid local heating from the thermistors, temperature measurements are never taken more often than every 30 seconds.

To reduce sedimentation and prevent convective flows, we used a density-matched mixture of Me-CC* with a critical concentration $c_c = 71\%$ cyclohexane by weight or mass fraction for which the critical temperature was $T_c = 46.640\,^\circ$C (see also ref. [1] for a detailed description of a ground-based experiment with density-matched Me-CC* and ref. [20] for a similar experiment with a critical mixture of Me-C very close to consolute critical point). The sample cell unit was filled to a slightly off critical concentration $|c - c_c| = 0.010 \pm 0.002$, which is well within the concentration range $|c - c_c| < 0.05$ where fluctuations are visible [1,21,22]. Although Me-CC* allows the density to be precisely matched, when quenched below $T_c = 46.640\,^\circ$C, slow sedimentation of the phase-separated droplets is still clearly visible in the microscopic field of view after several hours.

Thermostat

The thermal control system used air convection and radiation for heat transfer [18,19]. The cell and the larger copper housing were placed at the center of an aluminum cylinder of 18 cm length and 10 cm diameter with a foil heater glued to its exterior. Heat was continuously applied to the system with a computer-controlled power supply. The space between these cylinders was filled with air so that heat was exchanged with the inner copper housing only through radiation and convection. Two holes in the heating cylinder, aligned with the optical axis of the cell, allowed light to enter and leave the sample fluid. To prevent convective cooling of the sample cell windows, these holes were closed at both ends by optical windows. To provide a constant ambient temperature for the inner cylinder, two more thermal shields made of polystyrene of 7 cm thickness surrounded the heating cylinder. The walls of these rectangular polystyrene boxes were attached with silicone glue to provide an outer box with inner dimension 50 cm × 40 cm × 50 cm and an inner box with inner dimension 24 cm × 24 cm × 30 cm. These boxes provided two layers of shielding, except for the bottom which had only one layer, so that the optical support for the heating cylinder and the magnification lens could fit the boxes. The temperature of the air between these boxes was also computer controlled. The heater was placed near the top of the space between these thermal shields in order to create stable temperature gradient in this space such that the midpoint temperature was at an ambient temperature of approximately $(T_c - 5)\,^\circ$C, temperature fluctuation within $1\,^\circ$C. The thermostat control could achieve stability as high as 0.1 mK over 12 hours. Therefore, as mentioned in the Introduction, all the following analyses refer to a Me-CC* ternary mixture at $T = T_c + (1 + 0.1 - 0.3)$ mK.

Optics

In this work, we used a microscopy direct imaging method to record liquid-liquid fluctuations [18,19]. Our thermally shielded heating cylinder was placed on a optical bench shown schematically in fig. 1a (not to scale). We used a 100 W halogen lamp with a short coherence time and a longitudinal coherence length of $\approx 1\,\mu$m. As opposed to high spatial coherence of laser light sources, low-coherence light sources produce no speckle in the recorded image. Speckle is generated when an imaging system or a sample imparts a range of random path length differences, *e.g.* due to scattering, in mutually coherent photons that subsequently interfere at a detector [23]. A red filter was inserted between the halogen lamp and the collimator (see fig. 1a) to provide a monochromatic beam of light. A collimator made of two identical 7.8 mm diameter and 50 mm focal distance plan-convex lenses L_1 and L_2 produces a wide and parallel beam of monochromatic light. The 0.8 mm pinhole of the collimator is at the input focal point of L_2. The central portion of the collimated beam with a diameter of 1 cm travels through the sample cell unit (see fig. 1a).

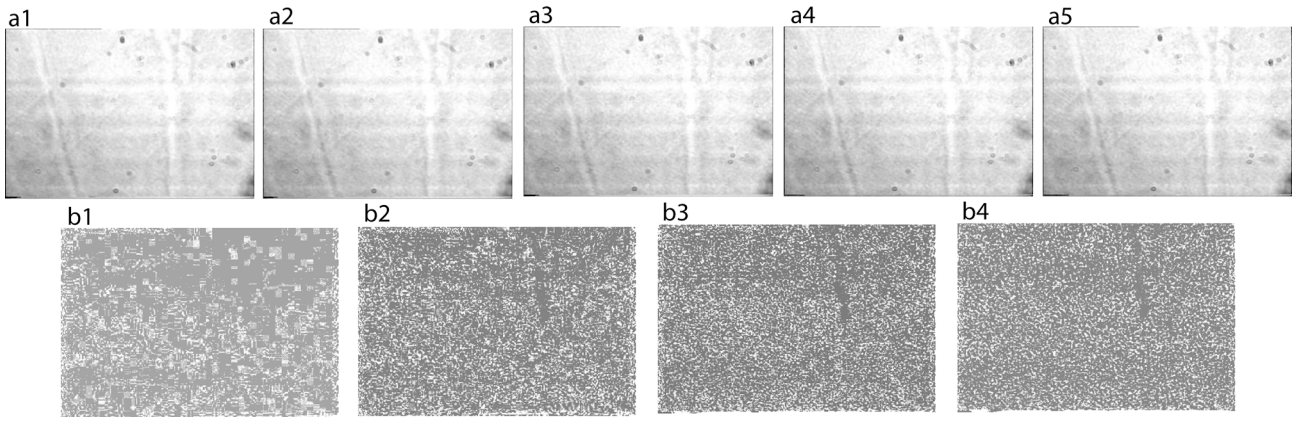

Fig. 2. (a) Images of equilibrium fluctuations near the consolute critical point of Me-CC* mixture acquired at $t = 0\,\mathrm{s}$ (a1), $t = 0.04\,\mathrm{s}$ (a2), $t = 0.4\,\mathrm{s}$ (a3), $t = 4\,\mathrm{s}$ (a4), $t = 40\,\mathrm{s}$ (a5). The height of the visualized sample was 1.5 mm. The strong background light and the weak scattering signal make the recorded images of equilibrium fluctuations look similar. (b) Fluctuation images obtained by subtracting the reference image (a1) from images taken at different delay times $\Delta t = 0.04\,\mathrm{s}$ (b1), $\Delta t = 0.4\,\mathrm{s}$ (b2), $\Delta t = 4\,\mathrm{s}$ (b3), $\Delta t = 40\,\mathrm{s}$ (b4). The subtraction removes the stationary background and emphasizes the local density fluctuations.

The sample cell unit was placed near the focal point of the high quality Olympus Zuiko 50 mm f/1.8 compound lens L_3. The position of Olympus lens L_3 was adjusted with a translation stage such that the field of view was near the output window of the cell. The sample cell position is adjusted along the optical axis by moving the bottom support using the translation stage of the heating cylinder that also contains the sample cell unit. The light input to the heating cylinder passes through a small glass covered hole and the output light travels through the lens L_3. The space between the cylinder and the lens L_3 is filled with a polystyrene spacer that allows for relative movement along the optical axis of the cell in order to adjust the position of the object plane. The maximum scattering angle, limited by the aperture of the Me-CC* cell, is about $\theta = 16.7$ degrees, which gives an effective numerical aperture $\mathrm{NA} = n\sin(\theta) = 0.29$ in air. A 8-bit monochromatic Sony XC-75CE CCD camera with a chip sensor of 7.95 mm × 6.45 mm and 752 pixels × 582 pixels was placed about 1 m from L_3. Based on Abbe's resolution formulas, the lateral resolution is $\lambda/(2\mathrm{NA}) \approx 1\,\mu\mathrm{m}$ for the red-filtered light used in our experiments. Additionally, the depth of focus was $\lambda/(2\mathrm{NA})^2 \approx 1.9\,\mu\mathrm{m}$.

The height of the visualized sample was 1.5 mm, which was mapped onto the 582 pixels of the CCD sensor (see fig. 2a). Since we cropped the rectangular images of 752 pixels × 582 pixels to 512 pixels × 512 pixels, the actual size of the visualized sample was $w \approx 1.3\,\mathrm{mm}$. As a result, the minimum wave vector in Fourier space was $q_{\min} = 2\pi/w \approx 48\,\mathrm{cm}^{-1}$. Given the dimension of the CCD sensor, it results that the magnification factor of the optical setup shown in fig. 1a was about 4.3. We tested our optical setup by visualizing images of phase-separated droplets (see fig. 1b).

Experimental protocol

The cell was first mechanically shaken by hand and then heated above T_c to approximately 50 °C where the Me-CC* mixture was allowed to sit for at least 12 hours so that it was thoroughly mixed by diffusion [18,19]. The temperature was then decreased toward the critical point in steps or temperature quenches, ΔT, that were decreased in magnitude as we approached T_c. Far from and above $T_c = 46.640\,^\circ\mathrm{C}$, we used $\Delta T = 1\,\mathrm{K}$ temperature quenches, whereas closer to T_c the temperature quenches were decreased to $\Delta T = 1\,\mathrm{mK}$. Because the quenches often resulted in as much as a 20% undershoot we limited the temperature quenches to 1 mK.

The phase separation was relatively fast, producing high contrast spatial domains that grew over time (see fig. 1b), then the consolute critical point could be measured to within 1 mK accuracy by observing the image after each quench to see if the fluid phase-separated. The identification of the features in the images was verified by waiting for over 12 hours. We found that the images retained the same characteristics and the fluid did not phase-separate. After each quench, the temperature was allowed to equilibrate for at least 20 minutes before recording the images of concentration fluctuations.

At each temperature, bright field images were recorded for about 1 minute at 25 frames per second with and without a red filter. The recorded video images were time tagged to correlate with the temperature data that was also time tagged.

3 Image analysis

Differential dynamic microscopy method

We applied an image processing method developed for DDM to real space images acquired with the above-described optical setup (see fig. 2a) in order to investigate the dynamics of concentration fluctuations near the consolute critical point of Me-CC*. In fig. 2a, the signal due to concentration fluctuations is barely visible because of the large bright background signal.

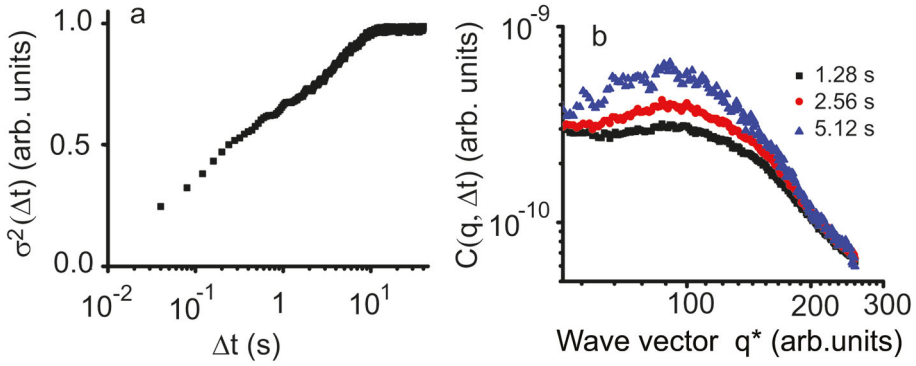

Fig. 3. (a) Equilibrium concentration fluctuations in critical Me-CC* mixture cause an increase of intensity fluctuation variance $\sigma^2(\Delta t)$. For small delay times Δt, the variance of intensity fluctuations is small since the images are correlated and a significant fraction of the scattering signal is also subtracted when removing the stationary background. When the time delay Δt increases, the two subtracted images become progressively uncorrelated and produced a $\sigma^2(\Delta t)$ plateau. (b) The azimuthal average of image structure function $C(q, \Delta t)$ plotted *versus* the reduced wave vector q^* for different values of the delay time $\Delta t = 1.28\,\mathrm{s}$ (squares), $\Delta t = 2.56\,\mathrm{s}$ (circles), and $\Delta t = 5.12\,\mathrm{s}$ (triangles).

Since the background brings a static contribution to all spatial images in fig. 2a, by subtracting two images recorded at different times, Δt, it is possible to eliminate background contribution and emphasize the scattering contribution to concentration fluctuations. In fig. 2a the left panel is a reference image that was subtracted from those taken at later times. The image subtraction procedure can be repeated for different values of the delay time Δt as shown in fig. 2b. The time-independent background signal was removed in the difference images (fig. 2b), which allowed the visualization of the weaker, small-scale, signal associated with concentration fluctuations.

As discussed in refs. [10,11], the amplitude of the fluctuation-related signal increases with the delay time Δt, a dependence that can be quantitatively captured by the variance of the difference images. A time-delayed fluctuation image $\Delta I(\mathbf{x}, t, \Delta t)$ is the difference between two real space images separated by a delay time Δt and is defined as

$$\Delta I(\mathbf{x}, t, \Delta t) = I(\mathbf{x}, t + \Delta t) - I(\mathbf{x}, t),$$

where $I(\mathbf{x}, t)$ is the intensity detected at the pixel with position $\mathbf{x}$ on CCD camera (see fig. 2b).

Assuming that equilibrium fluctuations are stationary, *i.e.* the dynamical properties of the system depend only on the time delay Δt but not on the actual reference time t, then $\Delta I(\mathbf{x}, t, \Delta t)$ dependence on t can be dropped. As a result, the expected mean value $\overline{\Delta I(\mathbf{x}, \Delta t)}$ is equal to zero and the energy content of the intensity fluctuations can be quantified by the expected variance $\sigma^2(\Delta t)$, which is defined as

$$\sigma^2(\Delta t) = \int\int \overline{|\Delta I(\mathbf{x}, \Delta t)|^2} \mathrm{d}\mathbf{x}.$$

As shown in refs. [10,11], the variance $\sigma^2(\Delta t)$ of the fluctuating images $\Delta I(\mathbf{x}, \Delta t)$ for dynamically active systems is expected to increase with Δt as a consequence of the local concentration fluctuations. Figure 3a shows the increase of $\sigma^2(\Delta t)$ for concentration fluctuations near the consolute critical point of Me-CC* mixture from a small background value due to detector noise to a large saturation plateau due to the complete loss of spatial correlation between successive images.

The principles, advantages, and applications of DDM technique were explained in depth in refs. [10,11]. In order to access statistical details regarding the scattered light, the intensity fluctuations $\Delta I(\mathbf{x}, \Delta t)$ obtained from microscopy direct imaging were analyzed in Fourier space. Local concentration fluctuations determine refractive index disturbances that can be Fourier decomposed. Each Fourier component of the refractive index distribution acts as a periodic diffraction grating that scatters light. DDM theory [10,11] established a one-to-one relationship between the Fourier components of the measured light intensity and the sample refractive index. Dynamical changes in the sample are determined by computing the image correlation function [10,11]

$$G(\mathbf{q}, \Delta t) = \overline{I^*(\mathbf{q}, 0) I(\mathbf{q}, \Delta t)},$$

where $I(\mathbf{q}, \Delta t)$ is the Fourier transforms of $I(\mathbf{x}, \Delta t)$ and $I^*(\,)$ is the complex conjugate of $I(\,)$. The normalized image correlation function $g(\mathbf{q}, \Delta t) = G(\mathbf{q}, \Delta t)/G(\mathbf{q}, 0)$ is related to the characteristic diffusion time constant. Croccolo *et al.* [24] showed that a more robust estimator for the normalized image correlation function can be obtained through computing the expectated value of the Fourier power spectrum of light intensity fluctuations:

$$c(\mathbf{q}, \Delta t) = \overline{|I(\mathbf{q}, \Delta t)|^2},$$

which is called the image structure function. In dynamic light scattering [24], the image structure function $c(\mathbf{q}, \Delta t)$ is called photon structure function or time-dependent structure function. In a series of seminal papers on DDM, Cerbino and Trappe [10] and Giavazzi *et al.* [11] showed that, without prior knowledge about the relationship be-

tween the light intensity and the refractive index fluctuations, the image structure function is generally given by

$$c(\mathbf{q}, \Delta t) = A(\mathbf{q})[1 - g(\mathbf{q}, \Delta t)] + B(\mathbf{q}), \quad (1)$$

where $A(\mathbf{q})$ includes contributions from the scattering properties of the sample, the coherence of the light source, and the details of optical setup. $B(\mathbf{q})$ accounts for the noise of the detection system. Furthermore, the normalized correlation function $g(\mathbf{q}, \Delta t)$ for Brownian motion is

$$g(\mathbf{q}, \Delta t) = e^{-\Delta t/\tau(\mathbf{q})}, \quad (2)$$

where $\tau(\mathbf{q}) = (Dq^2)^{-1}$ is the characteristic diffusion time and D is the diffusion coefficient. The above eq. (1) for white-light direct imaging is strikingly similar to the equation for the time-dependent structure function from DLS [24]. However, as proved by Cerbino and Trappe [10], the coefficient $A(\mathbf{q})$ has a very complex expression and both its derivation and meaning for non-coherent light are significantly different from the derivation of the similar coefficient obtained by Trainoff and Cannell [25] for DLS.

Cerbino and Trappe [10] showed that previous knowledge of $A(\mathbf{q})$ and $B(\mathbf{q})$ is not necessary for performing direct imaging experiments. We used eq. (1) with $A(\mathbf{q})$, $B(\mathbf{q})$, and $\tau(\mathbf{q})$ as fitting parameters to extract the correlation time of fluctuations from the image structure function. Additional information, such as the mutual mass diffusion coefficient D, was then extracted from the fluctuation correlation time $\tau(\mathbf{q})$ (see refs. [10,11]).

Because of the azimuthal symmetry exhibited by the image structure function $c(\mathbf{q}, \Delta t)$, we only retained and used its azimuthal average over thin rings with a width of $q_{\min} = 2\pi/w \approx 48\,\mathrm{cm}^{-1}$ (see fig. 3b):

$$C(q, \Delta t) = \overline{c(\mathbf{q}, \Delta t)_{|q|}}.$$

The azimuthal average of image structure function $C(q, \Delta t)$ was truncated at $q^* = 50$ arb. units ($q = q_{\min} q^* \approx 2381\,\mathrm{cm}^{-1}$) to eliminate the contribution of the very large zero order of the power spectrum that overshadowed the rest of the image structure function. Instead of using an opaque circular mask in Fourier space to remove the zero-order component, others used a Fourier mask that allowed a smooth decrease to zero of the image structure function [11]. The dynamics of the system can be revealed analyzing the behavior of the image structure function $C(q, \Delta t)$ as a function of Δt. Typical $C(q, \Delta t)$ plots *versus* the delay time are presented in fig. 4a for different wave vectors q. Regardless the method used for eliminating the contribution of the very large zero order of the power spectrum from the azimuthal average of image structure function $C(q, \Delta t)$, the area under the curve, *i.e.* the variance $\sigma^2(\Delta t)$, increases with Δt, as seen in fig. 3a.

We extracted the three fitting parameters $A(q)$, $B(q)$, and $\tau(q)$ based on eq. (1). Similar to DLS experiments, we also plotted in fig. 4b the normalized correlation function $g(q, \Delta t)$ that shows a fair exponential decay of the normalized correlation function of fluctuations. Our data

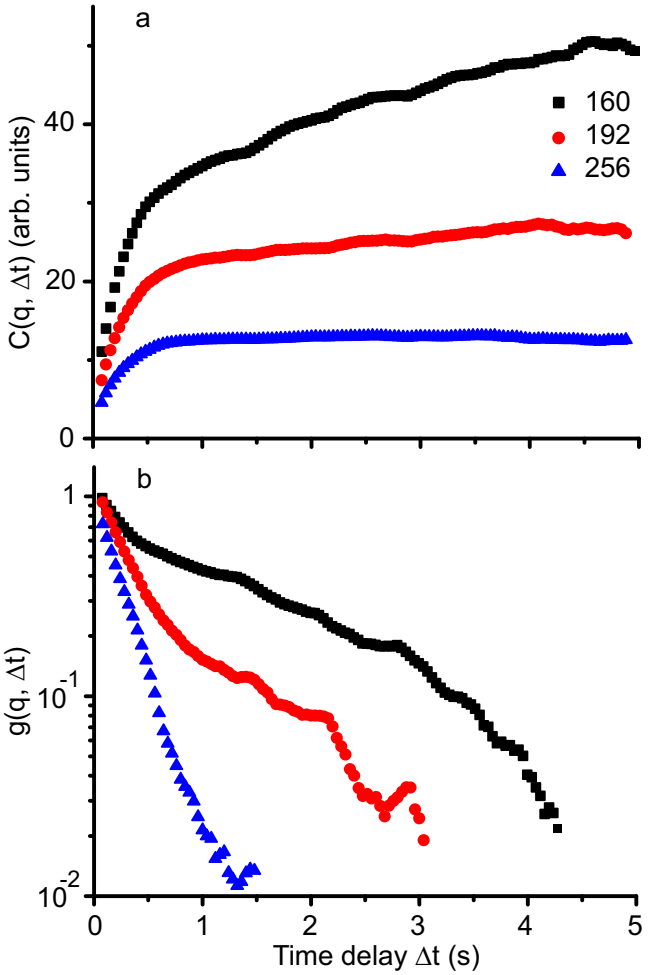

Fig. 4. (a) Evolution of the azimuthal average of image structure function, $C(q, \Delta t)$, as a function of the delay time Δt for three different values of wave vector $q^* = 256$ (black squares), $q^* = 192$ (red circles), and $q^* = 160$ (blue triangles). (b) Exponential decay of the normalized correlation function $g(q, \Delta t)$ corresponding to the same wave vectors as in (a).

show that the normalized correlation function can be well approximated by a single exponential given by eq. (2) similar to the results reported by Croccolo *et al.* [24, 26] for DLS experiments. For very short time delays, $\Delta t \to 0$, the normalized correlation function, $g(q, \Delta t)$, becomes unity while it decreases to zero for longer time delays (see fig. 4b). In our experiment, we recorded 1 minute of data at 25 frames/s, *i.e.* a minimum delay time $\Delta t = 0.04\,\mathrm{s}$, which is definitely smaller that 1/5 of the minimum characteristic time of fluctuations [24, 26–28]. We applied the above-described DDM image processing algorithm to overlapping sets of 128 successive images and computed successive image difference with a delay time from $\Delta t = 0.04\,\mathrm{s}$ to $N/2\Delta t = 5.12\,\mathrm{s}$ (see fig. 4). We cropped a 512 pixels × 512 pixels square image from the original 752 pixels × 582 pixels image such that the Fourier transform covers a range of wave vectors $q \in q_{\min}[1, N_{\mathrm{pix}}/2] \approx [48, 12189]\,\mathrm{cm}^{-1}$.

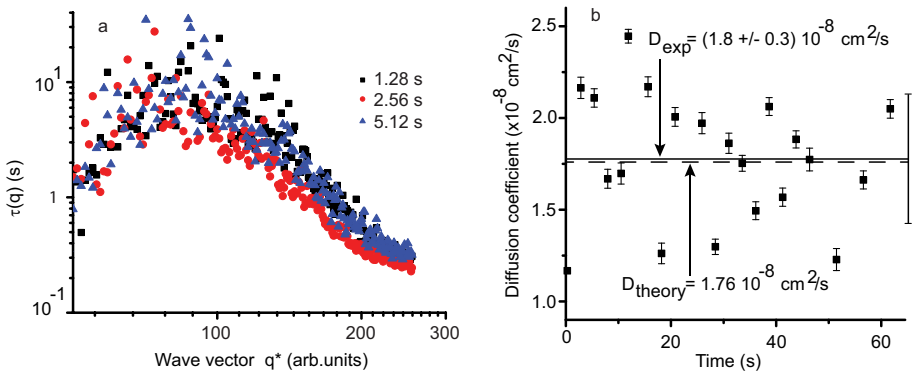

Fig. 5. (a) Experimentally determined characteristic decay time, $\tau(q)$, of concentration fluctuations plotted against the wave vector q^*. For large wave vectors, *i.e.* above a critical value $q^* \approx 85$, the existence of a power law behavior allowed mutual mass diffusion coefficient estimation based on eq. (3). (b) Experimentally determined mutual mass diffusion coefficient $D_{\rm exp} = (1.8 \pm 0.3) \cdot 10^{-8}\,{\rm cm}^2/{\rm s}$ (horizontal continuous line) obtained with the dynamic algorithm from the correlation time of fluctuations based on red-filtered bright field images. The vertical error bar on the right side of panel measures $0.3 \cdot 10^{-8}\,{\rm cm}^2/{\rm s}$ and represents one standard deviation of the average $D_{\rm exp}$. The horizontal dashed line at $D_{\rm theory} = 1.76 \cdot 10^{-8}\,{\rm cm}^2/{\rm s}$ represents the theoretically predicted mutual mass diffusion coefficient from Stokes-Einstein diffusion law with Kawasaki's correction.

4 Mutual mass diffusion coefficient

Experimental estimation of D

We computed the radial average of the azimuthal average of the image structure function $C(q, \Delta t)$ (see fig. 3b) for different delay times, Δt, which were multiple of the 1/25 s sampling rate. The saturation of $C(q, \Delta t)$ is determined by a significant decrease of correlation between images that are too far apart.

For a fixed time delay Δt between images, we computed the image differences $\Delta I(\boldsymbol{q}, t, \Delta t)$ that showed intensity fluctuations induced by local variations of the refractive index (see fig. 2b for red-filtered bright field images). The recording time t for each frame is the image's index multiplied by 1/25 s duration lapsed between successive frames. To reduce the noise related to the statistical properties of equilibrium fluctuations, we computed the average power spectrum over a set of 128 images with the same Δt (see fig. 2b). All our data sets showed clear saturation of the image structure function, which allowed us to accurately determine the correlation time of fluctuations τ.

The shape of the correlation time (see fig. 5a) suggests that at large wave vectors a power law could accurately fit the experimental data. In hydrodynamic regime ($q\xi \ll 1$) and for large wave vectors, the typical correlation time for equilibrium fluctuations should obey Kawasaki theory [29]

$$\tau^{-1} = Dq^2, \tag{3}$$

where D is the mutual mass diffusion coefficient. On the other hand, for $q\xi \gg 1$ (critical regime), the correlation time should scale as $\tau^{-1} \propto q^3$. The value of the critical correlation amplitude in methanol and pure cyclohexane is $\xi_0 = 0.238\,{\rm nm}$ from dynamic droplet model and $\xi_0 = 0.285\,{\rm nm}$ from mode-coupling theory [30]; $\xi_0 = 0.47\,{\rm nm}$ from refractive index experimental data [31]; $\xi_0 = (0.41 \pm 0.05)\,{\rm nm}$ from light scattering experiments [32]; and $\xi_0 = (0.387 \pm 0.035)\,{\rm nm}$ from turbidity measurements [20]. A detailed discussion about the ξ_0 value for Me-CC* can be found in Houessou *et al.* [1]. To our knowledge, Houessou *et al.* [1] is the only study on Me-CC* critical behavior, and the authors reported the critical amplitude ξ_0 in Me-CC* is somewhat different than of methanol and pure cyclohexane binary mixture. Here we considered $\xi_0 = 0.327\,{\rm nm}$ [1,33,20,34,35], which gives a correlation length of $\xi = 0.959\,\mu{\rm m}$ at 1 mK distance to T_c.

Since in our experiment the wave vector range is $48\,{\rm cm}^{-1} < q < 12189\,{\rm cm}^{-1}$, the product $q\xi$ is in the range $4.6 \cdot 10^{-3} < q\xi < 1.2$, which is definitely not $q\xi \gg 1$ as is required for the critical regime. As a result, our experimental data fall in the hydrodynamic regime where the correlation time of fluctuations scales according to eq. (3). We used a Levenberg-Marquardt least-square fitting algorithm to estimate the mutual mass diffusion coefficient D by fitting the correlation time data to eq. (3) with a fixed exponent of 2 for the wave vector. The range q^* that gave the best goodness of the fit was 90–150.

For each individual set of images over which we determined the mutual mass diffusion coefficient, D, using eq. (3) the standard deviation of the fitting parameter D is quite good. For example, at $t = 0.28\,{\rm s}$ we found $D_{\rm exp} = (1.17 \pm 0.06) \cdot 10^{-8}\,{\rm cm}^2/{\rm s}$ and at $t = 11.88\,{\rm s}$ the mutual mass diffusion coefficient was $D_{\rm exp} = (2.45 \pm 0.04) \cdot 10^{-8}\,{\rm cm}^2/{\rm s}$. However, due to the large spread of the fitting values (see fig. 5b) for the mutual mass diffusion coefficient, its average value is $D_{\rm exp} = 1.8 \cdot 10^{-8}\,{\rm cm}^2/{\rm s}$ (see the horizontal continuous line in fig. 5b) with a standard deviation of $0.3 \cdot 10^{-8}\,{\rm cm}^2$.

Theoretical estimation of D

The diffusion relaxation time determined with the above-described image processing algorithm is related to the mu-

tual mass diffusion coefficient, D, through eq. (3) [36,37]. At critical point, the mutual mass diffusion coefficient, D, vanishes [5], a phenomenon known as critical slowing down of fluctuations [38]. Away from critical point, the mutual mass diffusion coefficient varies slowly with temperature whereas near the critical point it breaks down into a background contribution and a critical enhancement due to long-range correlations. Following Sengers *et al.* [7, 39–41], the mutual mass diffusion coefficient near the critical point is $D = D^b + \Delta D$, where D^b is its background contribution and ΔD is its critical enhancement.

Close to the critical point, the critical enhancement ΔD of the mutual mass diffusion coefficient obeys Stokes-Einstein diffusion law asymptotically [29,42]

$$\Delta D = R_D \frac{k_B T}{6\pi\eta\xi}, \tag{4}$$

where $k_B = 1.381\cdot10^{-23}$ J/K is Boltzmann's constant, η is the viscosity, R_D is a universal amplitude and ξ is the correlation length. The value of R_D slightly changes with the approximations made by different models. For example, from mode-coupling theory $R_D = 1.00$ [29,43], whereas memory and nonlocal effects lead to $R_D = 1.03$ [38]. The renormalization group theory led to a broader range from $R_D = 0.8$ to $R_D = 1.2$ [44] and a more precise estimation gave $R_D = 1.063$ [45,46]. Here we used $R_D = 1.05$ as in [46].

The background mutual mass diffusion coefficient D^b is given by [7,39–41]

$$D^b = \frac{k_B T}{16\eta_b\xi}\frac{1}{q_C\xi}, \tag{5}$$

where η_b is the background viscosity and q_C is a system-dependent constant. The background viscosity is given by Arrhenius equation [38]

$$\eta_b = A_\eta \exp(B_\eta/k_B T),$$

where the coefficients slightly vary with the experimental method used, *e.g.* $A_\eta = 2.431\cdot10^{-5}$ Pa s and $B_\eta = 1.333\cdot10^{-20}$ J in [47] whereas $A_\eta = 1.085\cdot10^{-5}$ Pa s and $B_\eta = 1.471\cdot10^{-20}$ J in [48]. In our calculations, we used the values $A_\eta = 2.0\cdot10^{-5}$ Pa s and $B_\eta = 1.21221\cdot10^{-20}$ J from Alekhin *et al.* [49].

The viscosity η has a very weak divergence

$$\eta = \eta_b (Q_0\xi)^{z_\eta}, \tag{6}$$

where Q_0 is a system-dependent amplitude and the critical viscosity exponent computed from the mode-coupling model [50,51] is $z_\eta = 0.0679 \pm 0.0007$ whereas from experimental data it is $z_\eta = 0.0690 \pm 0.0006$ [52]. The constant q_C can be determined from

$$Q_0^{-1} = e^{4/3}/2(q_C^{-1} + q_D^{-1}), \tag{7}$$

where q_D is a Debye cutoff wave vector and Q_0 covers a wide range of values from $Q_0^{-1} = (1.2 \pm 0.3)$ nm [53] to $Q_0^{-1} = (1.8 \pm 0.06)$ nm [54]. Following Oxtoby and Gelbart [55], we also assumed $q_D^{-1} \ll q_C^{-1}$ and found q_C from eq. (7), which gave us $0.632\,\text{nm} < q_C^{-1} < 0.949\,\text{nm}$.

Our calculations showed that for a critical temperature of $T_c = 46.640\,^\circ$C as estimated through our 1 mK quenches (see sect. 2), the background viscosity of Me-CC* was $\eta_b = 3.11462\cdot10^{-4}$ Pa s.

As discussed in sect. 4, the amplitude of critical fluctuations is $\xi_0 = 0.3265$ nm, which gives a correlation length of fluctuations (at 1 mK distance to T_c) of $\xi = \xi_0\epsilon^{-\nu} = 0.96\,\mu$m. From eq. (7), we get $0.632\,\text{nm} < q_C^{-1} < 0.949\,\text{nm}$ (assuming $q_D = 0$ [55]), which leads to a negligible background mutual mass diffusion coefficient of $6.09\cdot10^{-12}\,\text{cm}^2/\text{s} < D^b < 9.136\cdot10^{-12}\,\text{cm}^2/\text{s}$ (see eq. (5)).

We also computed the critical contribution to mutual mass diffusion coefficient from eq. (4) by using the viscosity scaling law given by eq. (6) and found that it varies between $\Delta D = 5.2\cdot10^{-9}\,\text{cm}^2/\text{s}$ (for $Q_0^{-1} = 1.2\,\text{nm}$) and $\Delta D = 5.4\cdot10^{-9}\,\text{cm}^2/\text{s}$ (for $Q_0^{-1} = 1.8\,\text{nm}$).

Therefore, the theoretically estimated value of the mutual mass diffusion coefficient is $D_{\text{theory}} \approx 5.3\cdot10^{-9}\,\text{cm}^2/\text{s}$ while the experimental average of $D_{\text{exp}} = (1.8 \pm 0.3)\cdot10^{-8}\,\text{cm}^2/\text{s}$ as obtained from the correlation time of fluctuations in red-filtered images (see fig. 3a). Because of the significant difference between the D_{exp} and the D_{theory} values obtained from Stokes-Einstein diffusion law, we also estimated the contribution of Kawasaki correction of eq. (4) (see refs. [38,39])

$$\Delta D = R_D \frac{k_B T}{6\pi\eta\xi} K(q\xi)(1 + (q\xi/2)^2)^{z_\eta/2}, \tag{8}$$

where $K(x) = 3/(4x^2)(1 + x^2 + (x^3 - x - 1)\arctan x)$ is Kawasaki's function [29,36,42].

In our experiment, the product $x = q\xi$ is in the range $4.6\cdot10^{-3} < q\xi < 1.2$, which is definitely not $q\xi \gg 1$ (as it is required for the critical regime), but is large enough to warrant the use of the crossover formula given by eq. (8). We found that at the critical wave vector $q_c^* \approx 85$, *i.e.* $q_c = q_{\min}q^* \approx 4047\,\text{cm}^{-1}$ (see fig. 5a) $K(q_c\xi = 0.388) \approx 3.28$, which changes the theoretically estimated value of the mutual mass diffusion coefficient to $D_{\text{theory}} \approx 1.76\cdot10^{-8}\,\text{cm}^2/\text{s}$ (see the dashed line in fig. 5b). With Kawasaki's correction of Stokes-Einstein diffusion law, the experimental and theoretical values of mutual mass diffusion coefficient are close to each other.

5 Conclusions

We used a microscopy direct imaging method to visualize thermal fluctuations in a density-matched ternary mixture of methanol, cyclohexane, and partially deuterated cyclohexane (Me-CC*) near its consolute critical point. We determined the correlation time of concentration fluctuations using a dynamic differential microscopy image processing method.

For large wave vectors, the correlation time of fluctuations $\tau(q)$ obeys Kawasaki's theory (see eq. (3)), which allowed us to estimate the mutual mass diffusion coefficient

D. The average experimental value $D_{\rm exp} = (1.8 \pm 0.3) \cdot 10^{-8}\,{\rm cm}^2/{\rm s}$ (continuous line in fig. 5b) obtained from the red-filtered images agrees with our theoretically estimated values for the mutual mass diffusion coefficient range from $D_{\rm theory} = 1.76 \cdot 10^{-8}\,{\rm cm}^2/{\rm s}$ based on Stokes-Einstein diffusion law with Kawasaki's correction (see eq. (8)).

S.A. Oprisan acknowledges the National Science Foundation CAREER award IOS 1054914. This work was supported by NASA grants NAG3-1906 and NAG3-2447 to J.J. Hegseth. J.J. Hegseth gratefully acknowledges CNRS support. C. Lecoutre, Y. Garrabos and D. Beysens acknowledge CNES support.

References

1. C. Houessou, P. Guenoun, R. Gastaud, F. Perrot, D. Beysens, Phys. Rev. A **32**, 1818 (1985).
2. D. Beysens, P. Guenoun, F. Perrot, Phys. Rev. A **38**, 4173 (1988).
3. C. Knobler, N.-C. Wong, J. Phys. Chem. **85**, 1972 (1981).
4. C. Domb, *The Critical Point: A Historical Introduction To The Modern Theory Of Critical Phenomena* (Taylor and Francis Ltd, 1996).
5. H. Stanley, *Introduction to Phase Transitions and Critical Phenomena* (Oxford University Press, 1987).
6. R. Griffiths, J. Wheeler, Phys. Rev. A **2**, 1047 (1970).
7. J. Sengers, J. Shanks, J. Stat. Phys. **137**, 857 (2009).
8. D. Cannell, Phys. Rev. A **12**, 225 (1975).
9. J. Le Guillou, J. Zinn-Justin, Phys. Rev. Lett. **39**, 95 (1977).
10. R. Cerbino, V. Trappe, Phys. Rev. Lett. **100**, 188102 (2008).
11. F. Giavazzi, B. Brogioli, V. Trappe, T. Bellini, R. Cerbino, Phys. Rev. E **80**, 031403 (2009).
12. P. Kaplan, V. Trappe, D. Weitz, Appl. Opt. **38**, 4151 (1999).
13. M. Valentine, A. Popp, P. Kaplan, D. Weitz, Opt. Lett. **26**, 890 (2001).
14. L.G. Wilson, V.A. Martinez, J. Schwarz-Linek, J. Tailleur, G. Bryant, P.N. Pusey, W.C.K. Poon, Phys. Rev. Lett. **106**, 018101 (2011).
15. V. Martinez, R. Besseling, O. Croze, J. Tailleur, M. Reufer, J. Schwarz-Linek, L. Wilson, M. Bees, W. Poon, Biophys. J. **103**, 1637 (2012).
16. P.J. Lu, F. Giavazzi, T.E. Angelini, E. Zaccarelli, F. Jargstorff, A.B. Schofield, J.N. Wilking, M.B. Romanowsky, D.A. Weitz, R. Cerbino, Phys. Rev. Lett. **108**, 218103 (2012).
17. M. Reufer, V.A. Martinez, P. Schurtenberger, W.C.K. Poon, Langmuir **28**, 4618 (2012).
18. A. Oprisan, *Fluctuations, Phase Separation and Wetting Films near Liquid-Gas Critical Point*, PhD thesis (University of New Orleans, 2006).
19. J.J. Hegseth, A. Oprisan, Y. Garrabos, D. Beysens, Phys. Rev. E **90**, 022127 (2014).
20. R. Kopelman, R. Gammon, M. Moldover, Phys. Rev. A **29**, 2048 (1984).
21. P. Guenoun, F. Perrot, D. Beysens, Phys. Rev. Lett. **63**, 1152 (1989).
22. P. Guenoun, R. Gastaud, F. Perrot, D. Beysens, Phys. Rev. A **36**, 4876 (1987).
23. J. Dainty, *Laser speckle and related phenomena*, *Topics in Applied Physics* (Springer-Verlag, 1984).
24. F. Croccolo, D. Brogioli, A. Vailati, M. Giglio, D. Cannell, Ann. N.Y. Acad. Sci. **1077**, 365 (2006).
25. S. Trainoff, D. Cannell, Phys. Fluids **14**, 1340 (2002).
26. F. Croccolo, D. Brogioli, A. Vailati, M. Giglio, D. Cannell, Appl. Opt. **45**, 2166 (2006).
27. F. Croccolo, D. Brogioli, A. Vailati, M. Giglio, D. Cannell, Phys. Rev. E **76**, 041112 (2007).
28. F. Croccolo, H. Bataller, F. Scheffold, J. Chem. Phys. **137**, 234202 (2012).
29. K. Kawasaki, Ann. Phys. (N.Y.) **61**, 1 (1970).
30. C. Sorensen, R. Mockler, W. O'Sullivan, Phys. Rev. A **16**, 365 (1977).
31. C. Hartley, D. Jacobs, R. Mockler, W. O'Sullivan, Phys. Rev. Lett. **33**, 1129 (1974).
32. Y. Yosida, Phys. Lett. A **65**, 161 (1978).
33. A. Oprisan, B. Bayley, S. Oprisan, J. Hegseth, Y. Garrabos, C. Lecoutre, D. Beysens, *Thermal fluctuation exponents for two near-critical point systems*, in *SPIE, Visual Information Processing XIX*, Vol. **7701**, edited by Z.-u. Rahman, S.E. Reichenbach, M.A. Neifeld (SPIE, 2010).
34. D. Jacobs, Phys. Rev. A **33**, 2605 (1986).
35. R. Behrends, U. Kaatze, M. Schach, J. Chem. Phys. **119**, 7957 (2003).
36. A. Kostko, M. Anisimov, J. Sengers, Phys. Rev. E **76**, 021804 (2007).
37. H. Swinney, D. Henry, Phys. Rev. A **8**, 2586 (1973).
38. H. Burstyn, J. Sengers, J. Bhattacharjee, R. Ferrell, Phys. Rev. A **28**, 1567 (1983).
39. J. Sengers, Int. J. Thermophys. **6**, 203 (1985).
40. J. Sengers, *Effects of critical fluctuations on the thermodynamic and transport properties of supercritical fluids*, in *Supercritical Fluids: Fundamentals for Application*, edited by E. Kiran, J.M.H. Levelt Sengers (Kluwer Academic, Dordrecht, 1994) pp. 231–271.
41. J. Sengers, J. Luettmer-Strathmann, *The critical enhancements*, in *Properties of Fluids*, edited by J.H. Dymond, J. Millat, C.A. Nieto de Castro (Cambridge University Press, Cambridge, UK, 1995) pp. 131–159.
42. L. Mistura, Nuovo Cimento B **12**, 35 (1972).
43. A. Onuki, Phys. Rev. E **55**, 403 (1997).
44. P. Hohenberg, B. Halperin, Rev. Mod. Phys. **49**, 435 (1977).
45. R. Folk, G. Moser, Phys. Rev. Lett. **75**, 2706 (1995).
46. J. Luettmer-Strathmann, *Thermodiffusion in the critical region*, in *Thermal Nonequilibrium Phenomena in Fluid Mixtures*, edited by K. Werner, S. Wiegand, Vol. **584** of *Springer Lecture Notes in Physics* (Springer, Berlin, Heidelberg, 2002) pp. 24–37.
47. H. Burstyn, J. Sengers, Phys. Rev. A **25**, 448 (1982).
48. H. Leister, J. Allegra, G. Allen, J. Chem. Phys. **51**, 3701 (1969).
49. A. Alekhin, O. Bilous, Ukr. J. Phys. **52**, 793 (2007).
50. H. Hao, *Aspects of Dynamic Critical Phenomena in a Single Component Fluid*, PhD thesis (University of Maryland, College Park, Maryland, 1991).
51. H. Hao, R. Ferrell, J. Bhattacharjee, Phys. Rev. E **71**, 021201 (2005).
52. R. Berg, M. Moldover, G. Zimmerli, Phys. Rev. E **60**, 4079 (1999).
53. A. Stein, J. Allegra, G. Allen, J. Chem. Phys. **55**, 4265 (1971).
54. C. Sorensen, Int. J. Thermophys. **3**, 365 (1982).
55. D. Oxtoby, W. Gelbart, J. Chem. Phys. **61**, 2957 (1974).